

Symmetry-Constrained Anomalous Transport in the Altermagnetic Material CuX_2 ($\text{X}=\text{F},\text{Cl}$)

Zhengxuan Wang,¹ Ruqian Wu,^{2,*} Chunlan Ma,³ Shijing Gong,⁴
Shuaikang Zhang,¹ Guangtao Wang,¹ Tianxing Wang,¹ and Yipeng An^{1,†}

¹College of Physics, Henan Normal University, Xixiang, Henan 453007, China

²Department of Physics and Astronomy, University of California, Irvine 92697, USA

³School of Physics and Technology, Suzhou University of Science and Technology, Suzhou 215009, China

⁴Department of Physics, East China Normal University, Shanghai 200062, China

(Dated: March 26, 2025)

Recently discovered, altermagnetism represents a third class of collinear magnets. These materials exhibit zero net magnetization, similar to antiferromagnets, but display anomalous transport properties resembling those of ferromagnets. Altermagnetic materials manifest various anomalous electronic transport phenomena, including the anomalous Hall effect, anomalous Nernst effect, and anomalous thermal Hall effect. Additionally, they exhibit magneto-optical Kerr and Faraday effects, previously considered exclusive to ferromagnetic materials. These anomalous transport phenomena are constrained by symmetry, as revealed by density functional theory (DFT) calculations. However, an effective model-based approach to verify these symmetry constraints remains unavailable. In this Letter, we construct a $k \cdot p$ model for d -wave altermagnets CuX_2 ($\text{X}=\text{F},\text{Cl}$) using spin space group representations and apply it to calculate the anomalous Hall effect. The symmetry-imposed transport properties predicted by the model are in agreement with the DFT results, providing a foundation for further investigation into symmetry-restricted transport phenomena in altermagnetic materials.

Introduction Recently, altermagnet have attracted widespread attention as a novel class of collinear magnets. Like conventional collinear antiferromagnets, altermagnet exhibit a net magnetization of zero. However, they exhibit characteristics akin to ferromagnetic materials in terms of charge and thermal transport, featuring anomalous Hall effect (AHE), anomalous Nernst effect (ANE) and anomalous thermal Hall effect (ATHE) [1]. Additionally, while systems with zero net magnetization are typically thought to be incapable of exhibiting the magneto-optical Kerr effect (MOKE) and magneto-optical Faraday (MOFE) effect, altermagnet demonstrate non-zero optical Hall conductivity and finite magneto-optical Kerr and Faraday angles [2].

In traditional collinear antiferromagnetic (AFM) systems, time-reversal and inversion symmetry (\mathcal{PT} symmetry) guarantees spin degeneracy, as represented by $\mathcal{PT}\varphi_{k\uparrow} = \varphi_{k\downarrow}$. This symmetry spans the entire Brillouin zone, preventing spin splitting. In altermagnetic systems, however, the combined rotational and time-reversal symmetry (\mathcal{RT} symmetry) replaces \mathcal{PT} symmetry, but the k -invariant subspace of \mathcal{RT} symmetry is limited to a part of the Brillouin zone. This allows spin splitting where \mathcal{RT} symmetry is broken. Another consequence of the breaking of \mathcal{PT} symmetry is the potential emergence of the anomalous Hall effect. AHE typically requires the breaking of time-reversal symmetry, which is why it is often associated with ferromagnetic materials. However, AHE can also emerge in systems with non-zero net magnetization when non-magnetic atoms break time-reversal symmetry, as observed in materials like RuO_2 , where it was initially referred to as the crystal Hall effect [1, 3, 4].

With further study of RuO_2 , the concept of altermagnetism, a new class of collinear magnets, was introduced. Altermagnets inherently break time-reversal symmetry, making the occurrence of AHE possible. In addition, due to the presence of \mathcal{RT} and \mathcal{P} symmetry operations, the components of the anomalous Hall conductivity in different directions are subject to symmetry constraints. For instance, in the case of RuO_2 under the $M_{001}\mathcal{T}$ symmetry, the AHC σ_{xy} component is zero.

ANE [5] and ATHE [6] are thermoelectric analogs of the AHE, exhibiting similar symmetry dependence [7–14]. Like AHE, both ANE and ATHE arise from the breaking of time-reversal symmetry and are closely related to the system’s spin-orbit coupling. Systems that exhibit AHE typically also show the ANE and ATHE, making these properties defining characteristics of altermagnets. In particular, the ATHE and ATHE, like AHE, is closely linked to the system’s symmetry and demonstrates significant temperature dependence, further distinguishing altermagnetic materials from traditional AFM systems [1]. Similarly, the non-zero off-diagonal optical conductivity, as well as the magneto-optical Kerr effect and magneto-optical Faraday effect, represent unique properties of altermagnet. These magneto-optical effects provide additional signatures that set altermagnets apart from AFM materials [2, 15].

In this Letter, we investigate the CuX_2 ($\text{X}=\text{F},\text{Cl}$) system, which crystallizes in space group No. 14. Throughout the main text, we take CuF_2 as a representative example, while the corresponding calculations for CuCl_2 are provided in the Supporting Information. Firstly, we employed first-principles calculations to obtain the band

structure of CuF_2 , and examined the spin splitting of its valence band on the k_x - k_y and k_z - k_y planes, which are not protected by \mathcal{RT} symmetry. Subsequently, we constructed a $k \cdot p$ model based on the group representation of the spin space group of CuF_2 to verify the symmetry-constrained phenomena of the anomalous Hall effect. Finally, we calculated the anomalous electrical and photoelectrical transport properties of CuF_2 .

The electronic structure calculations were performed using the projector augmented wave (PAW) method as implemented in the Vienna Ab Initio Simulation Package (VASP) [16, 17]. The exchange-correlation functional was treated within the generalized-gradient approximation (GGA) with the Perdew-Burke-Ernzerhof (PBE) parametrization [18]. The lattice parameters were fixed, and the atomic positions were fully relaxed until the forces on each atom were less than 0.001 eV/\AA . The energy cutoff was set to 500 eV , with a convergence criterion of 10^{-7} eV . A $15 \times 11 \times 11$ k -point grid was used for the Brillouin zone sampling. Following the self-consistent field (SCF) calculations, maximally localized Wannier functions were constructed by projecting onto s , p and d orbitals of Cu atoms as well as onto p orbitals of F atoms, using a uniform k -point mesh of $17 \times 13 \times 13$ and the WANNIER90 package [19]. Additionally, we utilized the `kdotp-generator` Python package to generate the $k \cdot p$ model.

CuF_2 has a monoclinic lattice structure with lattice constant $a = 3.33 \text{ \AA}$, $b = 4.61 \text{ \AA}$ and $c = 5.41 \text{ \AA}$, the interaxial angle $\alpha = \gamma = 90^\circ$ and $\beta = 120^\circ$, as illustrated in Fig 1.(a). The crystal structure of CuF_2 belongs to the $P2_1/c$ (No.14) space group. This space group is generated by the two symmetry operations $\{\mathcal{C}_{2y}\mathcal{T}|(0, 1/2, 1/2)\}$ and the inversion operation, \mathcal{P} . Upon reversing the magnetic moments of the two Cu atoms within the unit cell, the generating set of the system's symmetry group transforms to $\{\mathcal{C}_{2y}\mathcal{T}|(0, 1/2, 1/2)\}$ and \mathcal{P} symmetry, where \mathcal{T} represents the time-reversal operation. Based on the space group tables [20], we can readily determine the k -invariant subspace S of the $\{\mathcal{C}_{2y}\mathcal{T}|(0, 1/2, 1/2)\}$ symmetry operation, as illustrated in Fig 1.(b). For k points belonging to S , the relation $\{\mathcal{C}_{2y}\mathcal{T}|(0, 1/2, 1/2)\}\varphi_{n\mathbf{k}\uparrow} = \varphi_{n\mathbf{k}\downarrow}$ holds true, resulting in the degeneracy of spin-up and spin-down states, as shown in Fig 1.(c). In contrast, for k points not belonging to S , the spin-up and spin-down states $\varphi_{n\mathbf{k}\uparrow}$ and $\varphi_{n\mathbf{k}\downarrow}$ are not protected by the $\{\mathcal{C}_{2y}\mathcal{T}|(0, 1/2, 1/2)\}$ operation and are susceptible to spin splitting, as depicted in Fig 1.(d). For the k_x - k_y and k_z - k_y planes, CuF_2 can be identified as a prototypical d-wave altermagnet with spin-momentum locking, as shown in Fig 1.(e) and (f).

The model Hamiltonian Due to the breaking of \mathcal{PT} symmetry, the altermagnet cannot be fully described by their space group or magnetic space group. For instance, in the CuF_2 system, it belongs to 14.79 (BNS number) magnetic space group, but the irreducible representation of this

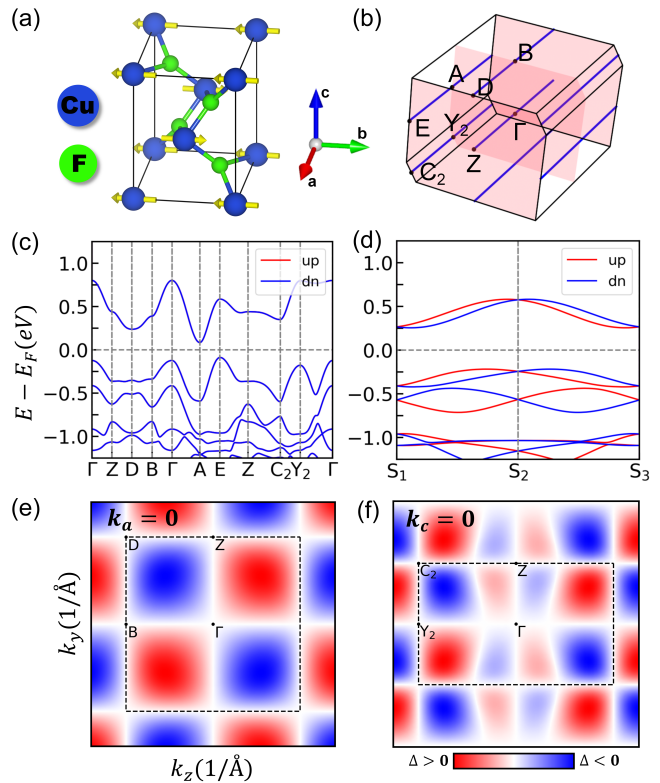


FIG. 1. (a), (b) The crystal structure and the Brillouin zone of CuF_2 respectively. The red face and blue line represent the k -invariant subspace of symmetry $\{\mathcal{C}_{2y}\mathcal{T}|(0, 1/2, 1/2)\}$. (c), (d) The band structure along the path which \mathbf{k} belong and does not belong to the invariant subspace of the symmetry operation $\{\mathcal{C}_{2y}\mathcal{T}|(0, 1/2, 1/2)\}$, respectively. $S_1 = (0, -1/2, 1/2)$, $S_2 = (0, 0, 1/2)$ and $S_3 = (0, 1/2, 1/2)$. (e) and (f) show the spin splitting in the k_z - k_y plane and k_x - k_y plane, respectively. The dash lines indicate the boundaries of the first Brillouin zone, and the colors correspond to $\Delta = \varepsilon_{\uparrow} - \varepsilon_{\downarrow}$.

magnetic space group at the Γ point is one-dimensional, which contradicts the results obtained from our DFT calculations. Therefore, for altermagnets, we must use a spin space group with more symmetry operations to describe the symmetry constraints and construct a model based on it. The CuF_2 system belongs to the spin group 14.1.2.3.L, which has four symmetry operations. At the Γ point, it has two two-dimensional irreducible representations connecting the spin-up and spin-down states, as shown in Table I.

To obtain all the symmetries of 14.1.2.3.L, we construct the $k \cdot p$ model based on the two degenerate spin-up and spin-down states at the valence band maximum at the Γ point, which are represented by Γ_1 . The constructed $k \cdot p$ Hamiltonian is given by:

| | Operation 1 | | | Operation 2 | | | Operation 3 | | | Operation 4 | | |
|------------|---|---|---|--|---|---|---|--|---|--|--|---|
| | Rotation | Spin Rotation | Tau | Rotation | Spin Rotation | Tau | Rotation | Spin Rotation | Tau | Rotation | Spin Rotation | Tau |
| | $\begin{pmatrix} 1 & 0 & 0 \\ 0 & 1 & 0 \\ 0 & 0 & 1 \end{pmatrix}$ | $\begin{pmatrix} 1 & 0 & 0 \\ 0 & 1 & 0 \\ 0 & 0 & 1 \end{pmatrix}$ | $\begin{pmatrix} 0 \\ 0 \\ 0 \end{pmatrix}$ | $\begin{pmatrix} -1 & 0 & 0 \\ 0 & -1 & 0 \\ 0 & 0 & -1 \end{pmatrix}$ | $\begin{pmatrix} 1 & 0 & 0 \\ 0 & 1 & 0 \\ 0 & 0 & 1 \end{pmatrix}$ | $\begin{pmatrix} 0 \\ 0 \\ 0 \end{pmatrix}$ | $\begin{pmatrix} -1 & 0 & 0 \\ 0 & 1 & 0 \\ 0 & 0 & -1 \end{pmatrix}$ | $\begin{pmatrix} -1 & 0 & 0 \\ 0 & -1 & 0 \\ 0 & 0 & -1 \end{pmatrix}$ | $\begin{pmatrix} 0 \\ \frac{1}{2} \\ \frac{1}{2} \end{pmatrix}$ | $\begin{pmatrix} 1 & 0 & 0 \\ 0 & -1 & 0 \\ 0 & 0 & 1 \end{pmatrix}$ | $\begin{pmatrix} -1 & 0 & 0 \\ 0 & -1 & 0 \\ 0 & 0 & -1 \end{pmatrix}$ | $\begin{pmatrix} 0 \\ \frac{1}{2} \\ \frac{1}{2} \end{pmatrix}$ |
| Γ_1 | $\begin{pmatrix} 1 & 0 \\ 0 & 1 \end{pmatrix}$ | | | $\begin{pmatrix} 1 & 0 \\ 0 & 1 \end{pmatrix}$ | | | $\begin{pmatrix} 0 & i \\ -i & 0 \end{pmatrix}$ | | | $\begin{pmatrix} 0 & i \\ -i & 0 \end{pmatrix}$ | | |
| Γ_2 | $\begin{pmatrix} 1 & 0 \\ 0 & 1 \end{pmatrix}$ | | | $\begin{pmatrix} -1 & 0 \\ 0 & -1 \end{pmatrix}$ | | | $\begin{pmatrix} 0 & i \\ -i & 0 \end{pmatrix}$ | | | $\begin{pmatrix} 0 & -i \\ i & 0 \end{pmatrix}$ | | |

TABLE I. This table lists the symmetry operations of the CuF₂ material in the spin space group 14.1.2.3.L, along with their spin group representations. The rotation operation matrices are written in the lattice coordinate system, while the spin rotation operations are written in the Cartesian coordinate system.

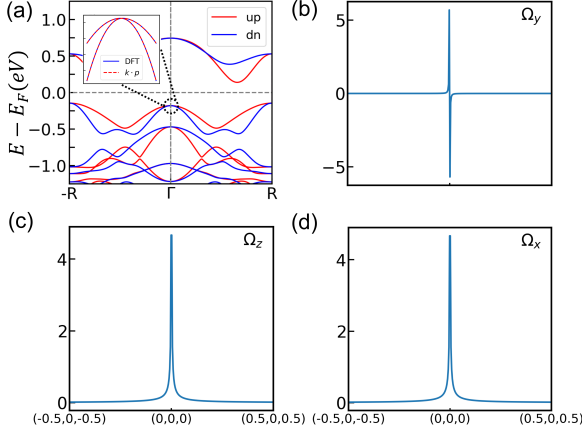


FIG. 2. (a) The band structure along the diagonal direction of the Brillouin zone passing through the Γ point. The inset shows a comparison between the $k \cdot p$ model and DFT calculations near the Γ point. (b), (c), and (d) are the Berry curvatures Ω_y , Ω_x , and Ω_z calculated on the $k_y = 0$ plane using the $k \cdot p$ model.

$$\begin{aligned}
H(\mathbf{k}) = & (c_0 + c_4 k_y + c_8 k_x^2 + c_{12} k_x k_z + c_{13} k_y^2 + c_{17} k_z^2) \sigma_0 \\
& + (c_1 k_x + c_5 k_z + c_9 k_x k_y + c_{14} k_y k_z) \sigma_1 \\
& + (c_2 k_x + c_6 k_z + c_{10} k_x k_y + c_{15} k_y k_z) \sigma_2 \\
& + (c_3 k_x + c_7 k_z + c_{11} k_x k_y + c_{16} k_y k_z) \sigma_3
\end{aligned} \quad (1)$$

where $\sigma_0, \sigma_1, \sigma_2, \sigma_3$ are the Pauli matrices. We fit this Hamiltonian along the diagonal direction of the Brillouin zone with the DFT-derived energy bands, and the fitting result is shown in the small inset of Fig 2.(a). For a two-band model, we can always decompose the Hamiltonian into the following form:

$$H(\mathbf{k}) = \varepsilon_0(\mathbf{k}) + \mathbf{h}(\mathbf{k}) \cdot \boldsymbol{\sigma} \quad (2)$$

where $\mathbf{h}(\mathbf{k})$ is the non-diagonal term of the Hamiltonian decomposed into a vector form with Pauli matrices. From this, we can obtain the Berry curvature in a simple way:

$$\Omega_z(\mathbf{k}) = -\frac{1}{2\hbar^3} \mathbf{h}(\mathbf{k}) \cdot \frac{\partial \mathbf{h}(\mathbf{k})}{\partial k_x} \times \frac{\partial \mathbf{h}(\mathbf{k})}{\partial k_y} \quad (3)$$

Based on this, we calculated Ω_{xy} , Ω_{yz} , and Ω_{zx} on the $k_y = 0$ plane, with the results shown in Fig 2(b)-(d). It is clear that under the $M_{010}\mathcal{T}$ symmetry operation, Ω_{zx} is always an odd function, and its integral over the Brillouin zone is always zero. This intriguing distribution of the Berry curvature arises from the $\mathcal{T}M_{010}$ symmetry operation inherent in CuF₂, which directly leads to Ω_y always being an odd function along the k_y direction. This can be easily derived from both the Berry curvature's Kubo formula and the aforementioned equations. This leads to the vanishing of the anomalous Hall conductivity component σ_{zx} .

Anomalous transport properties Alter-magnetic materials exhibit anomalous transport properties that distinguish them from AFM. These anomalies include non-zero anomalous Hall conductivity (AHC), anomalous Nernst conductivity (ANC), and anomalous thermal Hall conductivity (ATHC) in the absence of net magnetization. The intrinsic origin of these anomalous transport phenomena in alter-magnetic materials can be attributed to the non-zero Berry curvature integral, which arises from the energy splitting between up and down spin states in the Brillouin zone. Since these three transport properties share the same underlying symmetry, we focus on the AHC to discuss how symmetry affects these properties. The AHC, ANC and ATHC can be expressed as [21–23]:

$$\sigma_{xy}^{\text{AHC}} = -\frac{e^2}{\hbar} \int \frac{d^3 \mathbf{k}}{(2\pi)^3} \Omega_z(\mathbf{k}) \quad (4)$$

$$\alpha_{xy}^{\text{ANC}} = \int \frac{\varepsilon - \mu}{eT} \left(-\frac{\partial f}{\partial \varepsilon} \right) \sigma_{xy}^{\text{AHC}} d\varepsilon \quad (5)$$

$$k_{xy}^{\text{ATHC}} = \int \frac{(\varepsilon - \mu)^2}{e^2 T} \left(-\frac{\partial f}{\partial \varepsilon} \right) \sigma_{xy}^{\text{AHC}} d\varepsilon \quad (6)$$

where $\Omega_z(\mathbf{k})$ is the momentum-resolved Berry curvature, μ is the chemical potential, and $f =$

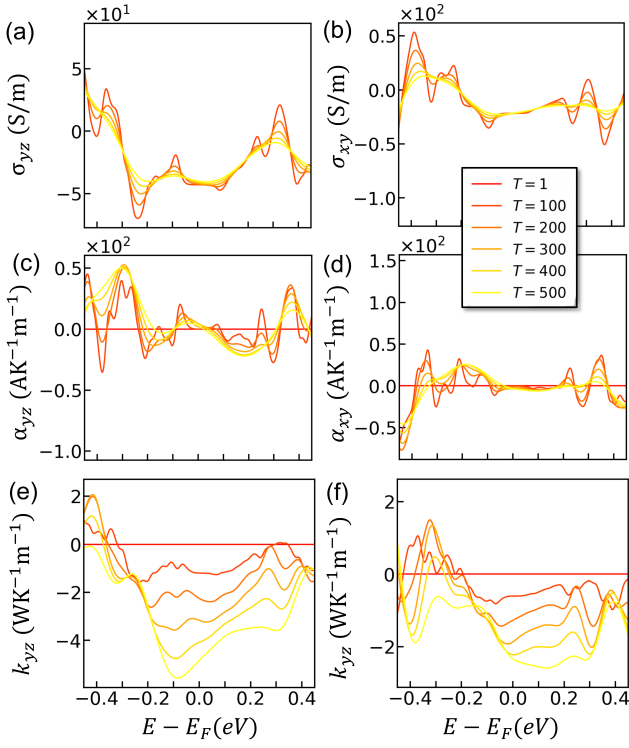


FIG. 3. Temperature-dependent behavior of various transport coefficients. Panels (a) and (b) show the anomalous Hall conductivity in the σ_{yz} and σ_{xy} directions, respectively, as a function of the Fermi energy. Panels (c) and (d) depict the anomalous Nernst conductivity in the α_{yz} and α_{xy} directions, respectively, as a function of the Fermi energy. Panels (e) and (f) illustrate the anomalous thermal Hall conductivity in the κ_{yz} and κ_{xy} directions, respectively, as a function of the Fermi energy. In all panels, The curves in all panels represent different temperatures, with each color corresponding to a specific temperature in Kelvin. Due to the sharp peak in anomalous Hall conductivity at $T = 1\text{K}$, the corresponding data has been placed in the supplementary information.

$1/[\exp((\varepsilon - \mu)/k_B T) + 1]$ is the Fermi-Dirac distribution function.

The AHC is strongly influenced by mirror symmetries, which cause certain components to vanish under specific symmetry operations. For instance, under the M_{001} symmetry, the components σ_{yz} and σ_{zx} will change sign, while σ_{xy} remains invariant. In this case, $\sigma_{yz} = \sigma_{zx} = 0$. For a combined time-reversal and mirror symmetry operation, such as $\mathcal{T}M_{001}$, only σ_{xy} is affected, and in this case, $\sigma_{xy} = 0$. This behavior of AHC leads to the disappearance of certain components of the Hall conductivity in systems with multiple mirror symmetries, such as RuO_2 , where the mirror symmetries are broken or restored depending on the magnetization direction[1].

In contrast, for the CuF_2 system, the unique mirror symmetry is coupled with time-reversal symmetry to form the combined $\{M_{010}\mathcal{T}|(0, 1/2, 1/2)\}$ operation. This operation always exists, regardless of the magneti-

zation direction. As a result, the components σ_{xy} and σ_{yz} are always non-zero, while σ_{zx} remains zero.

The same symmetry constraints apply to the ANC and the ATHC. Since both ANC and ATHC share the same symmetry structure as AHC, their behaviors with respect to changes in magnetization direction follow a similar pattern. The changes in magnetization direction can break or restore the mirror symmetries, leading to significant modulation of the ANC and ATHC. For instance, the periodic modulation of AHC with respect to magnetization direction also manifests in ANC and ATHC, as these properties are similarly influenced by the symmetry breaking.

Based on Equations (4)–(6), we have calculated the temperature-dependent AHC, ANC, and ATHE, with the results shown in Figure 3. At the true Fermi level, AHC is very small and shows little variation with temperature. However, through electron or hole doping, this value can be enhanced. Within the energy range relative to the true Fermi level (from -0.5 eV to 0.5 eV), σ_{yz} reaches a peak of -70.3 S/m at $T = 100\text{ K}$ and -0.23 eV , while σ_{xy} peaks at 53.2 S/m at -0.38 eV under the same temperature. For the thermoelectric coefficients, α_{yz} achieves a peak of $52.4\text{ AK}^{-1}\text{m}^{-1}$ at $T = 300\text{ K}$ and -0.29 eV , and α_{xy} peaks at $-77.2\text{ AK}^{-1}\text{m}^{-1}$ at $T = 200\text{ K}$ and -0.44 eV . The ATHC is directly proportional to temperature, with peak values occurring at $T = 500\text{ K}$. Specifically, κ_{yz} reaches a peak of $-5.59\text{ WK}^{-1}\text{m}^{-1}$ at -0.08 eV , and κ_{xy} peaks at $-2.64\text{ WK}^{-1}\text{m}^{-1}$ at 0.13 eV .

The MOKE and MOFE Alternating magnetic systems with a net-zero magnetic moment exhibit optical transport properties that are more similar to those of ferromagnetic systems. This is evidenced by phenomena such as a non-zero optical Hall conductivity, Magneto-optical Kerr effects and Magneto-optical Faraday effects. The optical conductivity can be given by the Kubo-Greenwood formula [24, 25],

$$\sigma_{xy}(\omega) = \frac{ie^2\hbar}{N_k\Omega_c} \sum_{\mathbf{k}} \sum_{n,m} \frac{f_{m\mathbf{k}} - f_{n\mathbf{k}}}{\varepsilon_{m\mathbf{k}} - \varepsilon_{n\mathbf{k}}} \times \frac{\langle \psi_{n\mathbf{k}} | v_\alpha | \psi_{m\mathbf{k}} \rangle \langle \psi_{m\mathbf{k}} | v_\beta | \psi_{n\mathbf{k}} \rangle}{\varepsilon_{m\mathbf{k}} - \varepsilon_{n\mathbf{k}} - (\hbar\omega + i\eta)}, \quad (7)$$

where Ω_c is the cell volume, N_k is the total number of k points used for sampling the Brillouin zone, $\psi_{n\mathbf{k}}$ and $\varepsilon_{n\mathbf{k}}$ are respectively the Wannier function and interpolated energy at band index n and momentum \mathbf{k} , $v_{\alpha,\beta}$ are velocity operators, $f_{n\mathbf{k}}$ is the Fermi-Dirac distribution function, $\hbar\omega$ is the photon energy, and η is an adjustable energy smearing parameter.

For the complex Kerr and Faraday angle, we adopt a simplified expression under the assumption of a small

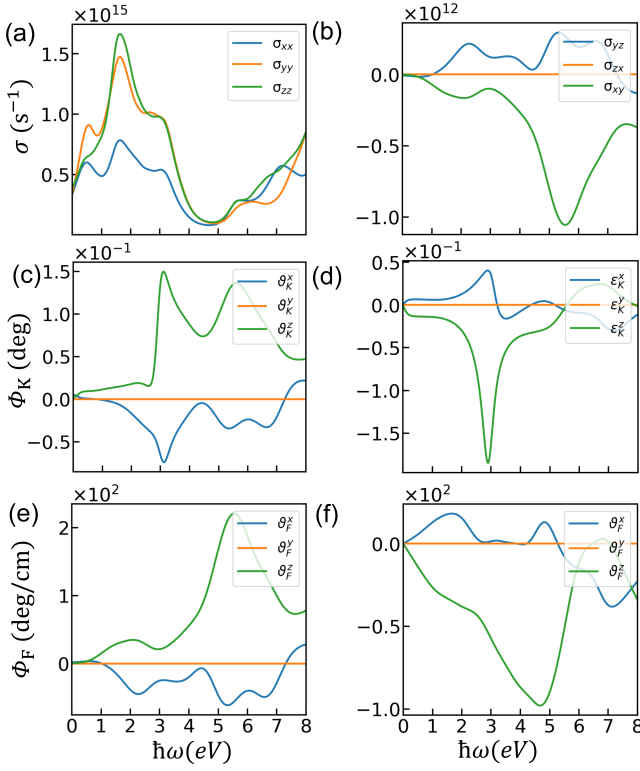


FIG. 4. Magneto-optical and optical conductivity properties. Panel (a) shows the diagonal component of the optical conductivity, while panel (b) presents the off-diagonal component. Panels (c) and (d) display the magneto-optical Kerr angle, with (c) showing the rotation angle and (d) showing the ellipticity. Panels (e) and (f) illustrate the magneto-optical Faraday angle, with (e) showing the rotation angle and (f) showing the ellipticity.

rotation angle [26–34]:

$$\phi_K^z = \vartheta_K^z + i\varepsilon_K^z \approx \frac{-\nu_{xyz}\sigma_{xy}}{\sigma_0\sqrt{1+i(4\pi/\omega)\sigma_0}}, \quad (8)$$

$$\phi_F^z = \vartheta_F^z + i\varepsilon_F^z \approx \frac{-\nu_{xyz}\sigma_{xy}}{\sqrt{1+i(4\pi/\omega)\sigma_0}} \frac{2\pi}{c}, \quad (9)$$

where $\sigma_0 = (\sigma_{xx} + \sigma_{yy})/2$. Detailed calculation steps can be found in the supplementary information.

Based on Equation (7), when the system exhibits mirror time-reversal ($\{M_{010}\mathcal{T}|(0, 1/2, 1/2)\}$) symmetry, the off-diagonal components of the optical conductivity tensor are constrained by this symmetry. In this case, the off-diagonal element σ_{zx} changes sign under $\{M_{010}\mathcal{T}|(0, 1/2, 1/2)\}$ symmetry, while σ_{xy} and σ_{yz} remain invariant, leading to the disappearance of σ_{zx} , as shown in Figure 4. Since both the Kerr and Faraday angles are derived from off-diagonal terms, their spectra exhibit similar behavior, i.e., $\phi_{Kky} = 0$ and $\phi_{Fky} = 0$, as shown in panels (c)-(f) of Figure 4. According to our calculations, the peak value of the Kerr angle in the z direction is approximately 0.15 deg at 3.09 eV, while

in the x direction, the peak value is around -0.07 deg at 3.18 eV. The peak value of the Faraday angle in the z direction is approximately 221 deg/cm at 5.54 eV, while in the x direction, the peak value is around 62 deg/cm at 5.31 eV.

In summary, altermagnets exhibit transport properties distinct from those of traditional collinear magnetic materials, and these transport properties are strictly constrained by symmetry. Moreover, neither the space group nor the magnetic space group can fully describe the symmetry constraints of altermagnets. We must use a spin space group with more comprehensive symmetry operations to construct a model of altermagnets with complete symmetry. This provides a method for further studying the symmetry-constrained transport properties of altermagnets.

We acknowledge funding from the National Natural Science Foundation of China (Grant Nos. 12274117, 62274066, and 62275074), the Program for Innovative Research Team (in Science and Technology) in University of Henan Province (Grant No. 24IRTSTHN025), the Natural Science Foundation of Henan (Grant No. 242300421214), and the HPCC of HNU. Work at UCI was supported by the U.S. DOE, Office of Science (Grant No. DE-FG02-05ER46237).

* wur@uci.edu

† ypan@htu.edu.cn

- [1] X. Zhou, W. Feng, R.-W. Zhang, L. Šmejkal, J. Sinova, Y. Mokrousov, and Y. Yao, Crystal thermal transport in altermagnetic RuO_2 , *Phys. Rev. Lett.* **132**, 056701 (2024).
- [2] X. Zhou, W. Feng, X. Yang, G.-Y. Guo, and Y. Yao, Crystal chirality magneto-optical effects in collinear antiferromagnets, *Phys. Rev. B* **104**, 024401 (2021).
- [3] L. Šmejkal, R. González-Hernández, T. Jungwirth, and J. Sinova, Crystal time-reversal symmetry breaking and spontaneous hall effect in collinear antiferromagnets, *Science Advances* **6**, eaaz8809 (2020).
- [4] Z. Feng, X. Zhou, L. Šmejkal, L. Wu, Z. Zhu, H. Guo, R. González-Hernández, X. Wang, H. Yan, P. Qin, *et al.*, An anomalous hall effect in altermagnetic ruthenium dioxide, *Nature Electronics* **5**, 735 (2022).
- [5] D. Xiao, Y. Yao, Z. Fang, and Q. Niu, Berry-phase effect in anomalous thermoelectric transport, *Phys. Rev. Lett.* **97**, 026603 (2006).
- [6] T. Qin, Q. Niu, and J. Shi, Energy magnetization and the thermal hall effect, *Phys. Rev. Lett.* **107**, 236601 (2011).
- [7] Y. Onose, Y. Shiomi, and Y. Tokura, Lorenz number determination of the dissipationless nature of the anomalous hall effect in itinerant ferromagnets, *Phys. Rev. Lett.* **100**, 016601 (2008).
- [8] Y. Shiomi, Y. Onose, and Y. Tokura, Extrinsic anomalous hall effect in charge and heat transport in pure iron, $\text{Fe}_{0.997}\text{Si}_{0.003}$, and $\text{Fe}_{0.97}\text{Co}_{0.03}$, *Phys. Rev. B* **79**, 100404 (2009).
- [9] Y. Shiomi, Y. Onose, and Y. Tokura, Effect of scattering on intrinsic anomalous hall effect investigated by Lorenz

- ratio, *Phys. Rev. B* **81**, 054414 (2010).
- [10] A. W. Smith, The transverse thermomagnetic effect in nickel and cobalt, *Phys. Rev. (Series I)* **33**, 295 (1911).
- [11] A. W. Smith, The hall effect and the nernst effect in magnetic alloys, *Phys. Rev.* **17**, 23 (1921).
- [12] W.-L. Lee, S. Watauchi, V. L. Miller, R. J. Cava, and N. P. Ong, Anomalous hall heat current and nernst effect in the $\text{CuCr}_2\text{Se}_4-x\text{Br}_x$ ferromagnet, *Phys. Rev. Lett.* **93**, 226601 (2004).
- [13] T. Miyasato, N. Abe, T. Fujii, A. Asamitsu, S. Onoda, Y. Onose, N. Nagaosa, and Y. Tokura, Crossover behavior of the anomalous hall effect and anomalous nernst effect in itinerant ferromagnets, *Phys. Rev. Lett.* **99**, 086602 (2007).
- [14] S. Onoda, N. Sugimoto, and N. Nagaosa, Quantum transport theory of anomalous electric, thermoelectric, and thermal hall effects in ferromagnets, *Phys. Rev. B* **77**, 165103 (2008).
- [15] L. Bai, W. Feng, S. Liu, L. Šmejkal, Y. Mokrousov, and Y. Yao, Altermagnetism: Exploring new frontiers in magnetism and spintronics, *Advanced Functional Materials* **34**, 2409327 (2024).
- [16] G. Kresse and J. Furthmüller, Efficiency of ab-initio total energy calculations for metals and semiconductors using a plane-wave basis set, *Computational Materials Science* **6**, 15 (1996).
- [17] P. E. Blöchl, Projector augmented-wave method, *Phys. Rev. B* **50**, 17953 (1994).
- [18] J. P. Perdew, K. Burke, and M. Ernzerhof, Generalized gradient approximation made simple, *Phys. Rev. Lett.* **77**, 3865 (1996).
- [19] A. A. Mostofi, J. R. Yates, Y.-S. Lee, I. Souza, D. Vanderbilt, and N. Marzari, wannier90: A tool for obtaining maximally-localised wannier functions, *Computer Physics Communications* **178**, 685 (2008).
- [20] M. I. Aroyo, A. Kirov, C. Capillas, J. M. Perez-Mato, and H. Wondratschek, Bilbao Crystallographic Server. II. Representations of crystallographic point groups and space groups, *Acta Crystallographica Section A* **62**, 115 (2006).
- [21] H. Ehrenreich and F. Spaepen, *Solid state physics*, Vol. 56 (Academic Press, 2001).
- [22] K. Behnia, *Fundamentals of thermoelectricity* (OUP Oxford, 2015).
- [23] H. van Houten, L. W. Molenkamp, C. W. J. Beenakker, and C. T. Foxon, Thermo-electric properties of quantum point contacts, *Semiconductor Science and Technology* **7**, B215 (1992).
- [24] A. A. Mostofi, J. R. Yates, Y.-S. Lee, I. Souza, D. Vanderbilt, and N. Marzari, wannier90: A tool for obtaining maximally-localised wannier functions, *Computer Physics Communications* **178**, 685 (2008).
- [25] J. R. Yates, X. Wang, D. Vanderbilt, and I. Souza, Spectral and fermi surface properties from wannier interpolation, *Phys. Rev. B* **75**, 195121 (2007).
- [26] W. Feng, G.-Y. Guo, J. Zhou, Y. Yao, and Q. Niu, Large magneto-optical kerr effect in noncollinear antiferromagnets Mn_3X ($\text{X} = \text{Rh, Ir, Pt}$), *Phys. Rev. B* **92**, 144426 (2015).
- [27] S. Wimmer, S. Mankovsky, J. Minár, A. N. Yaresko, and H. Ebert, Magneto-optic and transverse-transport properties of noncollinear antiferromagnets, *Phys. Rev. B* **100**, 214429 (2019).
- [28] X. Zhou, J.-P. Hanke, W. Feng, F. Li, G.-Y. Guo, Y. Yao, S. Blügel, and Y. Mokrousov, Spin-order dependent anomalous hall effect and magneto-optical effect in the noncollinear antiferromagnets Mn_3XN with $\text{X} = \text{Ga, Zn, Ag, or Ni}$, *Phys. Rev. B* **99**, 104428 (2019).
- [29] G. Y. Guo and H. Ebert, Band-theoretical investigation of the magneto-optical kerr effect in Fe and Co multilayers, *Phys. Rev. B* **51**, 12633 (1995).
- [30] P. Ravindran, A. Delin, P. James, B. Johansson, J. M. Wills, R. Ahuja, and O. Eriksson, Magnetic, optical, and magneto-optical properties of MnX ($\text{X} = \text{As, Sb, or Bi}$) from full-potential calculations, *Phys. Rev. B* **59**, 15680 (1999).
- [31] W. Feng, G.-Y. Guo, and Y. Yao, Tunable magneto-optical effects in hole-doped group-IIIa metal-monochalcogenide monolayers, *2D Materials* **4**, 015017 (2016).
- [32] X. Zhou, W. Feng, F. Li, and Y. Yao, Large magneto-optical effects in hole-doped blue phosphorene and gray arsenene, *Nanoscale* **9**, 17405 (2017).
- [33] F. Li, X. Zhou, W. Feng, B. Fu, and Y. Yao, Thickness-dependent magneto-optical effects in hole-doped gas and gase multilayers: a first-principles study, *New Journal of Physics* **20**, 043048 (2018).
- [34] X. Zhou, F. Li, Y. Xing, and W. Feng, Multifield-tunable magneto-optical effects in electron- and hole-doped nitrogen-graphene crystals, *J. Mater. Chem. C* **7**, 3360 (2019).